Numerical evidence that the impact of CCN and INP concentrations on mixed-phase clouds is observable with cloud radars

Junghwa Lee [1], Patric Seifert [1], Tempei Hashino [2], Maximilian Maahn [3], Fabian Senf [1], and Oswald Knoth [1]

[1]Leibniz Institute for Tropospheric Research (TROPOS), Leipzig, Germany
[2]Kochi University of Technology, Kochi, Japan
[3]Leipzig University, Leipzig, Germany

Correspondence: Junghwa Lee (lee@tropos.de)

Abstract. In this research, we delve into the influence of cloud condensation nuclei (CCN) and ice-nucleating particles (INP) concentrations on the morphology and abundance of ice particles in mixed-phase clouds, emphasizing the consequential impact of ice particle shape, number, and size on cloud dynamics and microphysics. Leveraging the synergy of the Advanced Microphysics Prediction System (AMPS) and the Kinematic Driver (KiD) model, we conducted simulations to capture cloud

5 microphysics across diverse CCN and INP concentrations. The Passive and Active Microwave radiative TRAnsfer (PAMTRA) radar forward simulator further augmented our study, offering insights into how the concentrations of CCN and INP affect radar reflectivities.

Our experimental framework encompassed CCN concentrations ranging from 10 to 5000 cm^{-3} and INP concentrations from 0.001 to 10 L^{-1}. Central to our findings are the observation that increased INP concentrations yield smaller ice particles, while

10 a surge in CCN concentrations leads to a subtle growth in their dimensions. Consistent with existing literature, our results spotlight plate-like crystals as dominant between temperatures of −20 to −16 °C. Notably, high INP scenarios unveiled a significant prevalence of irregular polycrystals. The Aspect Ratio (AR) of ice particles exhibited a decline with the rise in both CCN and INP concentrations, highlighting the nuanced interrelation between CCN levels and ice particle shape, especially its ramifications on the riming mechanism.

15 The forward-simulated radar reflectivities, spanning from −11.83 dBZ (low-INP, 0.001 L^{-1}) to 4.65 dBZ (high-INP, 10 L^{-1}), elucidate the complex dynamics between CCN and INP in determining mixed-phase cloud characteristics. Comparable differences in radar reflectivity were also reported from observational studies of stratiform mixed-phase clouds in contrasting aerosol environments. Our meticulous analysis of KiD-AMPS simulation outputs, coupled with insights into aerosol-driven microphysical changes, thus underscores the significance of this study in refining our ability to understand and interpret obser-

20 vations and climate projections.

1 Introduction

Clouds are still one of the most uncertain components of the global atmosphere system (Bony et al., 2015). Their formation and evolution occur on various spatio-temporal scales, which makes it virtually impossible to tackle them with single, unified

observational or simulation approaches (Kahn et al., 2023). Single sub-processes shall be studied individually and will only in
25 a later stage be the basis for an improved comprehensive understanding. Important components of a cloud's life cycle are, e.g.,
the cloud formation and the subsequent transitions from the liquid to the ice phase. The presence of the ice phase is an essential
prerequisite for the production of adequate amounts of precipitation in most regions on Earth (Mülmenstädt et al., 2015).
Nevertheless, for the initial formation of cloud droplets, as well as for the formation of ice crystals down to temperatures of
-38°C, aerosol particles are required for the phase transition by providing either a reservoir of cloud condensation nuclei (CCN)
30 or ice nucleating particles (INP), respectively (Morrison et al., 2012; Hoose and Möhler, 2012). The interplay of the abundance
of CCN and INP and the cloud evolution is an important pathway of aerosol-cloud interaction. Especially perturbations in the
concentration and type of CCN or INPs can potentially influence the formation and evolution of ice particles in mixed-phase
clouds.

There are strong indications given by both, observations and modeling approaches, that INP and CCN perturbations do have a
35 considerable impact on the mixed-phase cloud formation and evolution. Seifert et al. (2010) revealed increased fractions of ice-
containing clouds in dust-laden cloud environments over Central Europe. On a global scale, these findings were confirmed, e.g.,
by Zhang et al. (2018), using observations from the space-borne A-Train satellite constellation. Hemispheric contrasts in mixed-
phase clouds and their relationship to cloud turbulence and aerosol load were investigated in detail by Radenz et al. (2021),
who also concluded that a measurable impact of aerosol on mixed-phase cloud formation exists. Seifert et al. (2012) revealed
40 considerable impacts of a dust event on the simulation of clouds and precipitation patterns over Germany. Similar effects were
identified in a European-scale approach Barthlott and Hoose (2018). Fan et al. (2014) performed spectral bin simulations to
investigate the influence of CCN and INP on precipitation in two distinct mixed-phase orographic cloud scenarios characterized
by different cloud temperatures. The study revealed varying degrees of significance regarding the impacts of CCN and INP
on precipitation, with the INPs exhibiting a more pronounced effect in both cases. Furthermore, Fan et al. (2017) conducted a
45 sensitivity analysis where they systematically varied the concentrations of CCN and INP proxies across a wide range, spanning
from extremely low to extremely high concentrations, employing spectral bin modeling specifically tailored for orographic
mixed-phase clouds.

Also on a global scale, aerosol variations were found to be key for understanding the variability of mixed-phase clouds
(Atkinson et al., 2013). Recently, even the first closure studies bridging remote-sensing observations of CCN and INP with
50 those of cloud droplet concentration and ice crystal number concentration were brought underway (Ansmann et al., 2019;
Engelmann et al., 2021). However, simulations and observational approaches were to date rarely combined, which hinders
one to draw specific conclusions on aerosol effects on mixed-phase clouds. One key approach is to connect cloud-resolving,
aerosol-sensitive, ideally spectral-bin, models with forward operators in order to transfer simulation output into observation
space. By doing so, simulations for selected scenarios can be evaluated against real-world observations.

55 Given the complexity of spectral-bin modeling frameworks, it is essential to incorporate the most-relevant processes on
the one hand, but to constrain the environmental conditions to a maximum but still realistic state, on the other hand. Besides
number concentration, thus also particle habit should be incorporated into respective aerosol-cloud-interaction studies which
aim on a closure against observations. Ice particle shape plays a crucial role in determining the microphysical and radiative

properties of mixed-phase and ice clouds (Mishchenko et al., 1996; McFarquhar and Heymsfield, 1997). The diverse shapes

60   of ice particles influence their growth, aggregation, and riming processes, which in turn affect cloud lifetime, precipitation formation, and radiative energy transfer within the atmosphere (Magono and Lee, 1966; Heymsfield and Westbrook, 2010; Um and McFarquhar, 2011). The complexity and diversity of ice particle shapes present challenges for both cloud microphysics modeling and remote sensing of cloud properties. A comprehensive understanding of ice particle shape is essential for improving the accuracy of cloud microphysics models, remote sensing retrievals, and ultimately, climate predictions (Liou and

65   Ou, 2004; Tao et al., 2012; Chen and Liu, 2016; Vázquez-Martín et al., 2021). Despite its importance, the representation of ice particle shape in cloud microphysics models remains a significant challenge. Many models adopt simplified assumptions regarding ice particle shape, such as assuming all particles are spherical or using a limited set of predefined shapes (Mitchell, 1996; Morrison et al., 2005; Cotton et al., 2013). These simplifications can introduce uncertainties and biases in the simulated cloud properties and their interactions with radiation (Cotton et al., 2013; Eriksson et al., 2015). Furthermore, the complex

70   nature of ice particle shape and its dependence on factors such as temperature, supersaturation, and aerosol loading adds to the difficulty in accurately representing this aspect of cloud microphysics (Bailey and Hallett, 2009; Kanji et al., 2017).

Radar remote sensing is a valuable tool for observing ice particles in clouds, providing insights into their size, shape, and spatial distribution (Hogan et al. 2000; Westbrook and Illingworth, 2011). However, interpreting radar observations of ice particles requires a thorough understanding of the relationship between ice particle shape and the radar variables, such as

75   reflectivity and Doppler velocity (Hogan et al., 2012; Kneifel et al., 2015). Radar forward simulators, which generate synthetic radar observations based on cloud model outputs, can help bridge this gap by allowing researchers to systematically investigate the sensitivity of radar variables to different ice particle shapes and model assumptions (Matsui et al., 2019).

In this study, we utilize the Advanced Microphysics Prediction System (AMPS) coupled with the Kinematic Driver (KiD) to conduct idealized simulations of mixed-phase cloud microphysics (Hashino et al., 2007; Hashino et al., 2008; Hashino and

80   Tripoli, 2011a; Hashino and Tripoli, 2011b), incorporating a comprehensive representation of ice particle shapes and the effects of CCN and INP perturbations. AMPS is a state-of-the-art cloud microphysics model that has been specifically designed to capture the complex interactions between aerosols, cloud droplets, and ice particles with a habit prediction system (Hashino et al., 2007; Hashino et al., 2008; Hashino and Tripoli, 2011a. The AMPS model coupled with large-eddy simulations (LES) successfully reproduces features of mixed-phase clouds and has been compared to observations (Hashino et al., 2020; Ong et

85   al., 2022). To investigate the impact of ice particle shape on radar retrievals, we employ the Passive and Active Microwave radiative TRAnsfer (PAMTRA) radar forward simulator. PAMTRA is a versatile tool that can simulate passive and active microwave observations of the atmosphere, accounting for the scattering properties of various ice particle shapes (Mech et al., 2020). By combining the capabilities of AMPS and PAMTRA, this study aims to provide a comprehensive understanding of the role of ice particle number size distribution and shape in mixed-phase cloud microphysics and remote sensing retrievals

90   under varying CCN and INP conditions. Furthermore, we seek to evaluate the impact of ice particle shape assumptions and CCN/INP perturbations on the accuracy and reliability of cloud property retrievals from radar observations.

This paper is organized as follows. Sect. 2 briefly describes the Kinematic Driver (KiD) (Shipway and Hill, 2012) as the dynamical model and AMPS as the microphysics model. Sect. 3 give information on the initial thermodynamic condition and

experimental design for simulations. Sect. 4 shows the numerical simulation results for steady-state mixed-phase cloud cases
95 under varying CCN and INP scenarios. Finally, Sect. 5 concludes the paper with a summary of the results.

2 Model description and simulation setup

2.1 KiD (dynamic model)

The KiD model provides a framework for examining cloud microphysics, enabling us to assess and compare different parameterizations, which leads to a better understanding of cloud particle interactions and the influence of aerosols on cloud
100 development. The model's versatility allows its application in the study of various cloud types, including stratiform mixed-phase and convective clouds. It has significantly contributed to the enhancement of cloud microphysical parameterizations in larger-scale models (Klein et al., 2009; Shipway et al., 2012). These schemes include simple bulk microphysics models like 1-moment bulk models (Thompson et al., 2004) and even more complex schemes like the 2-moment scheme (Thompson et al., 2008; Morrison et al., 2009). In addition, the KiD model can accommodate comprehensive spectral-bin microphysics schemes,
105 such as the Tel-Aviv University bin microphysics scheme (Tzivion et al., 1987) and the AMPS. For more information, refer to Shipway and Hill (2012).

We emphasize the KiD framework's effectiveness in efficiently evaluating the performance of different microphysics schemes. Additionally, the KiD model functions as a valuable benchmarking tool, enabling researchers to evaluate and enhance cloud microphysics parameterizations. By comparing the results of various parameterizations within the KiD framework, inconsis-
110 tencies and areas for improvement can be identified and investigated.

2.2 AMPS (microphysics model)

In this study, we employed the Kinematic Driver model (KiD) in conjunction with the Advanced Microphysics Prediction System (AMPS) to simulate mixed-phase clouds. The AMPS model has been coupled with other dynamic models such as the University of Wisconsin-Nonhydrostatic Modeling system (Hashino and Tripoli, 2007; Hashino and Tripoli, 2008; Hashino
115 et al., 2020) and the Scalable Computing for Advanced Library and Environment (SCALE) large-eddy simulation model (Ong et al., 2022), demonstrating its capability to accurately predict mixed-phase clouds and exhibiting favorable comparisons with observational data. According to Hashino and Tripoli (2007, 2008, 2011a, 2011b), the Spectral Ice Habit Prediction System (SHIPS) in the AMPS microphysical model incorporates particle property variables (PPVs) to characterize the physical structure of ice particles. SHIPS continuously updates the PPVs for each mass bin in response to evolving ambient conditions,
120 ensuring accurate particle property diagnoses based on the PPVs. Given this capability, we conclude that AMPS is well-suited to investigate the impact of varying CCN and INP conditions on particle shape. The identification of ice particle type and crystal habit relies on various components, including mass content, length, and concentration. The habit diagnosis takes into account the crystal geometry and growth mode during the vapor deposition process.

For the identified particle type, an ice particle model is assigned, which encompasses a geometric shape surrounding the ice particle. Figure 1 presents the dimensions and sketches of monocrystals. This model plays a crucial role in providing a geometrically consistent framework for microphysical processes, which includes crystal habit information such as the a-axis length (representing the radius, l_a), the c-axis length (representing the height, l_c), and the d-axis length (representing the dendritic arm, l_d) of the three crystal habits: plate, columnar, and dendrite for monocrystals. In addition to the parameters used to identify different monocrystal habits, the AMPS model employs a PPV known as the extra crystalline structure number (n_exice), ranging from 0 to 1. If n_exice is greater than or equal to 0.5, it indicates that ice crystals in a given bin are polycrystals. Figure 2 displays the flowchart used to determine the ice habit. AMPS also uses the coordinates of the center of gravity (a_g, c_g) measured along the a- and c-axes from the center of the monocrystals as two PPVs to differentiate between planar and columnar polycrystals. If $a_\mathrm{g}/l_\mathrm{a}$ is greater than $c_\mathrm{g}/l_\mathrm{c}$ plus 0.5, the ice crystal is identified as a planar polycrystal (e.g., side plane), while if $c_\mathrm{g}/l_\mathrm{c}$ is greater than $a_\mathrm{g}/l_\mathrm{a}$ plus 0.5, the ice crystal is identified as a columnar polycrystal (e.g., bullet rosette). Any ice crystal that falls outside these ranges, such as a scale-like side plane, is classified as an irregular polycrystal. In the AMPS model, the volume of ice particles is denoted as V_cs, representing the sphere volume circumscribing the ice particle. The formulation for calculating V_cs depends on the particle type: for most ice particles, it is determined by the equation $k_s(l_\mathrm{a,sm})^3(1+\alpha^2)^{3/2}$, where $k_s = 4\pi/3$, and α represents the aspect ratio (AR) of the ice particle defined as the ratio of the vertical semiaxis length ($l_\mathrm{c,sm}$) to the horizontal semiaxis length ($l_\mathrm{a,sm}$). However, for graupel, it is computed using $k_s(l_\mathrm{a,sm})^3 \max(1,\alpha^3)$. In general, the AR of an object is the ratio of its width to its height. In this study, the AR of polycrystalline ice particles is determined by the ratio of the semi-axis lengths of the ice particle model, i.e., $\alpha = l_{c,\mathrm{sm}} / l_{a,\mathrm{sm}}$, while the AR of monocrystalline particles is determined by the ratio of the axis lengths, $\alpha = l_c / l_a$.

To explain more about ice particle habit, the ice crystal growth regime is determined based on the cumulative relative frequency of habits and a random number generator when the temperature falls below -20°C and the maximum dimension of the crystal is less than 20 μm. The growth regime is initially selected from polycrystalline, columnar, and planar hexagonal regimes. If the growth regime is polycrystalline, a random number determines whether it is columnar or planar polycrystalline. Furthermore, if it is polycrystalline, another random number determines the growth regime for a hexagonal monocrystal. This implies that small ice crystals can grow differently from the habit diagnosed at the beginning of the time step. Conversely, for temperatures above -20°C, it is assumed that polycrystals do not form. Once the maximum dimension exceeds 20 μm, the ice crystal is presumed to follow the growth of the diagnosed habit at the beginning of the time step.

2.3 PAMTRA (Radar forward Simulator)

The radar reflectivity factor, denoted as Z_e, characterizes the ability of an object, such as atmospheric precipitation, to reflect radar signals, enabling the identification and quantification of precipitation events. The magnitude of reflectivity depends on various factors, including the size, concentration, composition of the precipitation particles, and the frequency of the radar signal. To convert the model data into radar variables, we utilize PAMTRA, a powerful tool designed for simulating and retrieving microwave radiative properties in the atmosphere. Serving as a forward model, PAMTRA allows the interpretation of data from diverse passive and active microwave sensors, including radars and radiometers, used for observing and studying precipitation
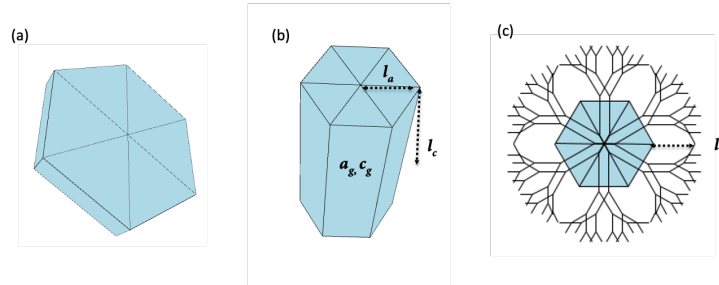
Figure 1. Diagnosis of the habit of the representative hydrometeor dimensions (l_a, l_c, and l_d) for monocrystals, including (a) hexagonal plate, (b) column, and (c) dendrite.

and other atmospheric phenomena. PAMTRA incorporates crucial factors such as cloud and precipitation scattering, and gas absorption, and facilitates comprehensive analysis of remote sensing data from satellite, airborne, and ground-based platforms.
160 Numerous studies have leveraged PAMTRA to investigate precipitation processes, cloud microphysics, and remote sensing of atmospheric variables, establishing it as an invaluable resource for researchers and atmospheric scientists engaged in the field of radiative transfer and remote sensing (Maahn et al., 2019; Ori et al., 2020; Schnitt et al., 2020; von Lerber et al., 2022).

PAMTRA offers a full-bin interface with several benefits, which can directly convert spectral-bin model data or in situ measurement for each size bin to radar variables. This conversion facilitates the transfer of crucial information, such as mass,
165 density, number concentration, terminal velocity, cross-sectional area, AR, and particle size distribution, without the need for further assumptions. In contrast, a bulk microphysics model provides hydrometeor mixing ratio in one-moment microphysics models (e.g., Baldauf et al., 2011) or mixing ratio and number concentration in two-moment microphysics models (e.g., Seifert and Beheng, 2006). Requring assumptions about particle size distribution, mass-size relations, and terminal velocity in PAMTRA. In the context of the spectral bin model AMPS, the terminal velocity for the sedimentation of a prognostic variable for
170 a specific bin is determined by considering the mass, concentration, and the particular type of PPVs within that bin (Hashino and Tripoli, 2007). Radar reflectivity factor z_e [mm^6 m^{-3}] is obtained by integrating the normalized particle size distribution (PSD) $n(D)$ over the entire range of particle sizes D,

$$z_e = \int 10^{18} \sigma_B(D) n(D) \frac{\lambda^4}{\pi^5 |K_w|^2} dD \qquad (1)$$

Where λ is the wavelength in meters, $|K_w|$ corresponds to the dielectric factor of water, and $\sigma_B(D)$ stands for the backscatter-
175 ing cross-section of individual hydrometeor particles in square meters (m^2). Typically, radar reflectivity is used in logarithmic units converted with $Z_e[dBZ] = 10 \log_{10} z_e[mm^6 m^{-3}]$.

It is standard practice to use the value for liquid water at centimeter wavelengths ($|K_w| = 0.93$ at Ka-band; Ulaby et al., 1981) regardless of whether ice or liquid clouds are observed. However, $|K_w|$ is also frequency-dependent. This study employs the Self-Similar Rayleigh-Gans approximation (SSRGA) parameterization proposed by Hogan et al. (2017) for the backscattering
180 cross-section $\sigma_B(D)$ calculation. This parameterization is determined by five dimensionless parameters: α_e, K, β, γ, and
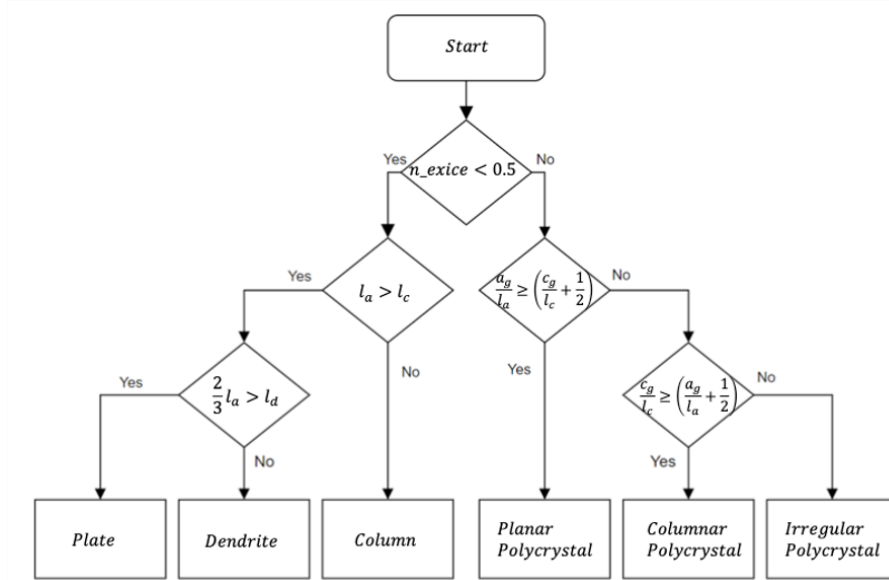
Figure 2. Flowchart depicting the diagnostic procedure for identifying ice particle habits in the AMPS.

ζ. The AR of the particles is represented by α_e, whereas K measures the mean mass distribution of the particle along the propagation direction and is referred to as the kurtosis parameter. The mass fluctuations around the mean mass distribution are described by β and γ, which represent the power law prefactor and exponent, respectively. ζ is a correction term for the power spectrum of the smallest wavenumber. We choose the SSRGA coefficients depending on the normalized particle rime mass
185 fraction following Maherndl et al. (2023).

3 Model description and simulation setup

3.1 Initial profile

We selected a 1D mixed-phase stratocumulus case for our experiments with the KiD-AMPS framework. To minimize the effects of the microphysics schemes, the temperature field is kept constant. The vertical velocity demonstrates repeated up/down
190 oscillation, and an additional vapor source is supplied to artificially recreate a quasi-steady stratocumulus condition. The vertical velocity is given as

$$w(z,t) = \begin{cases} w_1 \frac{z}{z_1} \left(1 - \exp\left[-\left(\frac{z-z_1}{z_2} \right)^2 \right] \right) \sin\left(\pi t/t_1 \right), & \text{if } z < z_1 \\ 0.0, & \text{otherwise} \end{cases} \tag{2}$$

and the additional forcing
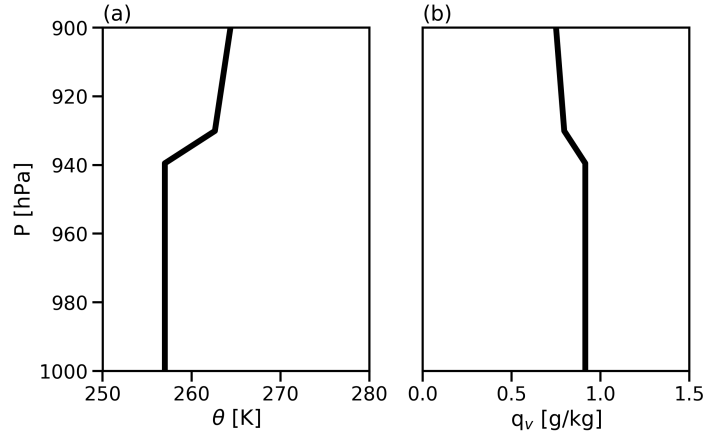
Figure 3. The initial condition of the (a) potential temperature Θ [K] and (b) specific humidity q_v [g/kg] profile in KiD-AMPS simulation.

$$\frac{dq}{dt}_{\text{add}}(z,t) = \frac{dq}{dt}_{\text{add}}(z,0) = \begin{cases} A\cos\left(\frac{1.25\pi}{2}\right), & \text{if } z < z_3 + z_4, \\ A\cos\left(\frac{z-z_3}{z_4}\frac{\pi}{2}\right), & \text{if } z_3 + z_4 < z < z_3 + 1.25z_4, \end{cases} \tag{3}$$

195   and A satisfies

$$\int_0^{z_5} \frac{dq}{dt}_{\text{add}}(z,0)dz = f_q/3600 \tag{4}$$

The parameters z_1, z_2, z_3, z_4, and z_5 are set to 450 m, 200 m, 400 m, 100 m, and 1000 m, respectively. Similarly, the values of ω_1, t_1, and f_q are set to 1.0 m/s, 600 s, and 5 mm/h, respectively. The initial potential temperature and specific humidity profile are displayed in Figure 3. This implies that the cloud's top region exhibits a temperature of approximately $-20\,^\circ\text{C}$, 200   whereas the lowermost part of the cloud shows a temperature of $-15\,^\circ\text{C}$.

3.2 Experimental designs (CCN/INP)

This study aimed to investigate the impact of varying initial concentrations of CCN and INPs on the formation and evolution of clouds. It is widely recognized that aerosols can significantly influence cloud formation and evolution, with their role in these processes depending on factors such as size, composition, and concentration. It should be noted that while aerosols can act as 205   a source of INPs, not all aerosols possess this capability. INPs are particular types of particles capable of initiating ice crystal formation at temperatures below 0°C. The precise composition and physical properties of INPs can considerably vary based on specific conditions, with mineral dust, biological particles (e.g., bacteria and fungi), and certain anthropogenic particles

(e.g., industrial emissions) being the most prevalent sources of INPs (Hoose and Möhler, 2012). For this research, we employ Ammonium Sulfate as CCN and assume that the insoluble portion of all aerosols consists of montmorillonite as INP sources.

210 Hashino et al. (2020) demonstrated that the volume-dependent Bigg's immersion method (Diehl and S.Wurzler, 2004) is to be well-suited for characterizing the ice nucleation process. Consequently, we adopt Bigg's immersion freezing method in this study as well. For further details on ice nucleation schemes, de Boer et al. (2010) (2013) and Hashino et al. (2020) can be referred to.

Within the AMPS model, the quantification of CCN is accomplished using a spectrum consisting of 40 bins, where each

215 bin contains prognostic CCN number concentrations. Aerosol particles are represented by lognormal size distributions, which provide comprehensive coverage of their size range. The particle size distribution is utilized to describe the aerosol distribution, and for each bin, the critical supersaturation value is individually computed. As the iteration proceeds, bins that exhibit a critical supersaturation below the threshold of environmental supersaturation are identified and subsequently transferred to the liquid spectrum. This methodology ensures the appropriate incorporation of bins in the liquid phase, leading to a faithful depiction of

220 cloud microphysics within the AMPS model. As previously mentioned, montmorillonite particle number concentration serves as an INP proxy for this simulation. For the present study, we conduct sensitivity analyses in this study by altering CCN and INP proxy concentrations across an extensive range, from extremely low to exceptionally high levels, as illustrated in Table 1. The initial CCN concentrations for these sensitivity simulations are set at 10, 50, 500, 1000, and 5000 cm^{-3} (denoted as CCN10, CCN50, CCN500, CCN1000, and CCN5000, respectively). For each CCN condition, simulations are carried out with

225 initial INP particle concentrations of 0.001, 0.1, and 10 L^{-1}, respectively, labeled as INP0.001, INP0.1, and INP10. A similar range for the experimental setup was also selected in the sensitivity study of Fan et al. (2017). The authors further emphasize that in heavily polluted regions like China and India, where CCN concentrations exceeding 1000 cm^{-3} are prevalent, such high values hold significant implications for precipitation extremes and water cycles. Choudhury and Tesche (2023) provides a comprehensive global multiyear dataset of height-resolved concentrations of cloud condensation nuclei (CCN) categorized

230 by aerosol types. These estimates are derived from the spaceborne lidar instrument aboard the Cloud-Aerosol Lidar and Infra-Red Pathfinder Satellite Observation (CALIPSO) satellite. Notably, recent studies demonstrate that the levels of extreme CCN concentrations in heavily polluted regions can exceed 5000 cm^{-3}. The selected INP range is well motivated with respect to the variability which can be found in existing in-situ and remote-sensing studies of INP concentrations. Specifically, we based the decision for the lowest value of INP concentration on the values reported for the free troposphere over the Southern-Ocean

235 site of Punta Arenas, Chile (Radenz et al., 2021). The selected maximum value of INP concentration of 10 L^{-1} can, e.g., be observed in the case of strong Saharan dust outbreaks in the Mediterranean region as was reported for instance by Ansmann et al. (2019). The range also agrees well with in-situ measurements, as reported by DeMott et al. (2010).

In total, we conducted 15 experiments, and from this set, we specifically selected 5 representative cases (EXP1–5) for detailed analysis in Section 4.1 of the Results (see Table 1). These selected cases encompass clean, pristine, and polluted

240 scenarios, achieved by varying the concentration of CCN and adjusting the concentration of INP to be 100 times smaller and 100 times larger than the commonly observed value of 0.1 L^{-1} in Arctic mixed-phase clouds. The results of the sensitivity test,

Table 1. Definition of the experiments EXP1–5 referred to in the remainder of this study. The simulations are conducted using various concentrations of CCN and INP aerosols.

		CCN [cm^{-3}]				
		10	50	500	1000	5000
	0.001	X	EXP3	X	X	X
INP [L^{-1}]	0.1	EXP4	EXP2	EXP5	X	X
	10	X	EXP1	X	X	X

covering all cases, will be presented in Section 4.2. Additionally, Section 4.3 will showcase the outcomes of coupling a typical EXP1–5 case with PAMTRA for radar retrieval analysis.

4   Results

4.1   Comparative analysis of CCN and INP effects on mixed-phase clouds

We analyze the evolution of cloud formations and the progression of hydrometeors by altering the initial CCN and INP concentrations. In this chapter, our primary focus will be on Cases EXP1–5 (see Table 1), which represent the most contrasting experimental scenarios among the 15 cases examined.

Figure 4 presents the temporal evolution of cloud development, specifically focusing on the average column value over time. This figure provides valuable insights into the progression of cloud formation in relation to the initial conditions, considering the variations in CCN and INP. In Figure 4(a), we present the effective diameter values of ice particles obtained from the simulations. In this study, the effective diameter of ice particles, denoted as $D_{\text{eff, ice}}$, is calculated using Equation 5.

$$D_{\text{eff, ice}} = 2\sqrt{V_{\text{cs}}/(\pi l_{c,\text{sm}})} \tag{5}$$

The mean effective diameters after $t = 100$ min for EXP1, EXP2, EXP3, EXP4, and EXP5 are 79 μm, 193 μm, 331 μm, 275 μm, and 346 μm, respectively. It is observed that as the concentration of INP increases, there is a corresponding decrease in the effective diameter of ice particles, as evident in EXP1, EXP2, and EXP3. Conversely, an increase in CCN concentration results in a slight increase in the effective diameter, as observed in EXP4 and EXP5. The simulated effective diameters of ice particles span a wide range, ranging from small values in the tens of microns to larger values in the range of thousands of microns. These findings are consistent with previous observations indicating effective diameters within the range of 300 μm to 800 μm (Morrison et al., 2011).

AMPS comprises two separate bin spectra. The first 40 bins represent the liquid phase and are categorized as either cloud or rain, while the next 20 bins represent the ice phase. The mixing ratio and number concentration of liquid and ice values are found to remain in a quasi-steady state, with the exception of EXP1. Moreover, the experimental results in Figure 4(b) for the number concentration of ice (N_{ice}) in EXP2, EXP4, and EXP5, ranging from 0.3 to 1.7 L^{-1} (gray zone), are in agreement with previous observations from Surface Heat Budget of the Arctic Ocean (SHEBA) campaign of mixed-phase clouds (Morrison
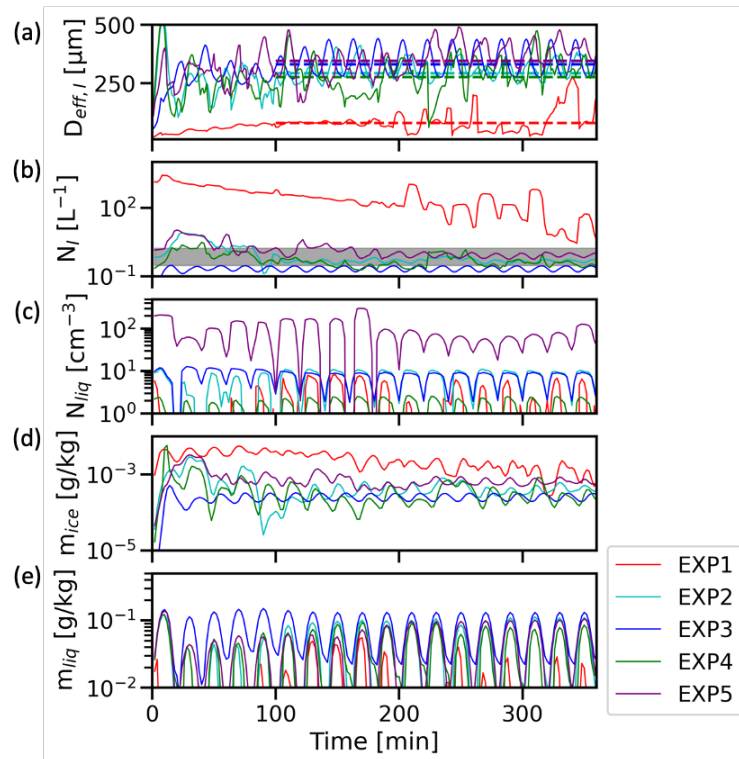
Figure 4. Time series of key variables: (a) effective diameter of ice crystals ($D_{eff, ice}$) with the dotted line representing the average value from 100 minutes, (b) ice number concentration (N_{ice}), (c) liquid number concentration (N_{liq}), (d) mixing ratio of ice (m_{ice}), and (e) mixing ratio of liquid (m_{liq}). The gray-shaded regions correspond to the ranges derived from observational data obtained during the SHEBA campaign

et al., 2011; Fridlind et al., 2012). These results further suggest that the experiment accurately represents typical mixed-phase clouds. Figure 4 indicates that as INP concentrations increase in EXP1, EXP2, and EXP3, both N_{ice} and m_{ice} significantly increase, while N_{liq} and m_{liq} decrease. Conversely, the mean m_{ice} is slightly higher in experiments with increased CCN (EXP4, EXP2, and EXP5) despite the higher N_{liq} and m_{liq}, consistent with findings from earlier studies employing 2-moment bulk
270 microphysics simulations (Solomon et al., 2018) and experimental investigations (Desai et al., 2019).

The impact of CCN and INP perturbations on cloud evolution is illustrated in Figure 5. It is observed that increasing CCN concentration can significantly affect the relationship between liquid water and ice mixing ratios. The ice water content is markedly higher as the concentration of INP concentration increases. In the high-INP scenario (EXP1), the conversion of water droplets into ice crystals occurs more rapidly and efficiently. Consequently, this case predicts almost fully glaciated
275 clouds. When the number of CCN increases, more cloud droplets are formed from within the reservoir of available water vapor. This can lead to an increase in the number concentration of cloud droplets within the cloud as shown in Figure 4(c), which can, in turn, reduce the size of individual cloud droplets. This reduction in droplet size increases the altitude of the cloud base and reduces the amount of precipitation, which can result in an increase in cloud water mass, given that the cloud is
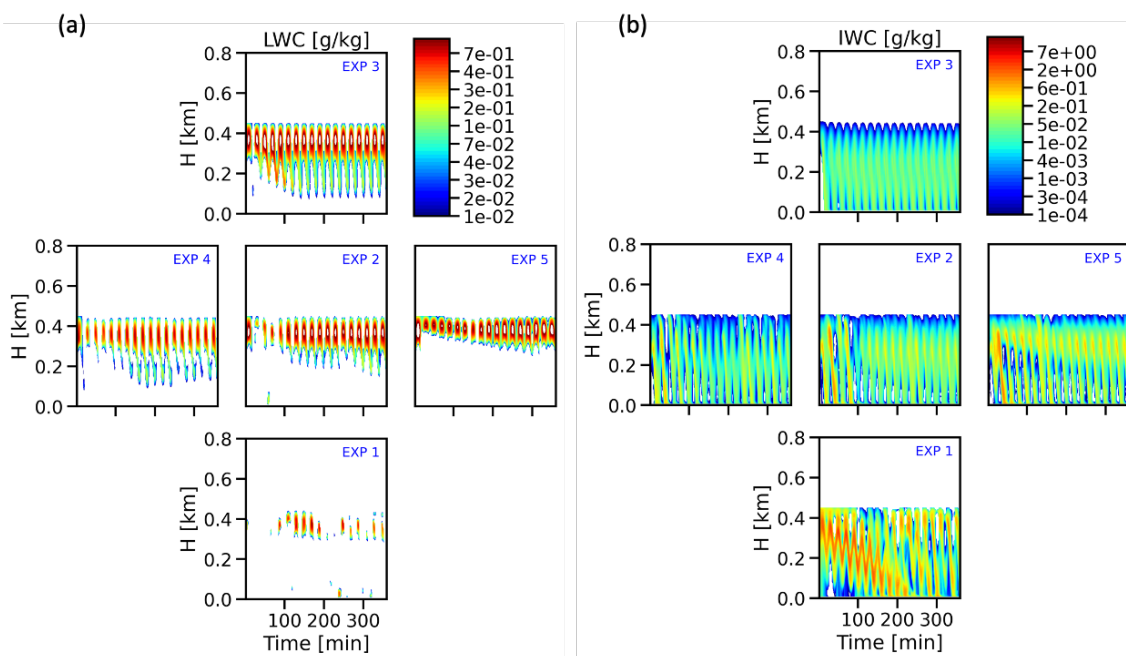
Figure 5. Vertical distribution comparison of (a) liquid water content (LWC) [g/kg] and (b) ice water content (IWC) [g/kg] across EXP1–5.

not already saturated with respect to the available water vapor. In summary, the alteration of cloud particle concentration due
280   to perturbations in the aerosol concentrations leads to adjustments in cloud and precipitation patterns, even in the absence of
cloud-dynamics interaction, as previously observed in studies by Seifert et al. (2012), Boucher et al. (2013), Heyn et al. (2017),
Possner et al. (2017), Solomon et al. (2018), and Zhang et al. (2018).

Next, we will investigate the response of the ice-phase processes of AMPS to the aerosol perturbations. In the AMPS model,
the mass of an ice crystal is partitioned into various process-oriented categories, including pristine crystal mass, aggregated
285   mass, riming mass, and melted water mass, which are tracked as PPVs. The bin components are created through microphysical
processes that act upon them, including vapor deposition onto ice crystals, which produce ice crystal mass, melting processes
which produce liquid mass, aggregation processes which generate aggregate mass, and riming processes which produce rime
mass. The sum of these four components makes up the total mass. In Figure 6, the mixing ratio of ice water content is presented
separately for the 4 ice-phase processes and for each of the 5 selected experiments. High concentrations of INPs lead to an
290   increased number concentration of ice particles (see Fig. 4) and consequently to increased ice water mass, as the presence of
INPs allows the formation of ice crystals to occur more readily, resulting in an increased number of collisions and coalescence
among the ice crystals. The results demonstrate that as the number of aerosols and concentration of INPs increase, there is a
corresponding increase in the frequency of aggregation due to the higher concentration of ice crystals that promote this process.
Conversely, it is observed that the occurrence of riming is reduced when there is a shortage of sustained supercooled liquid
295   layers.
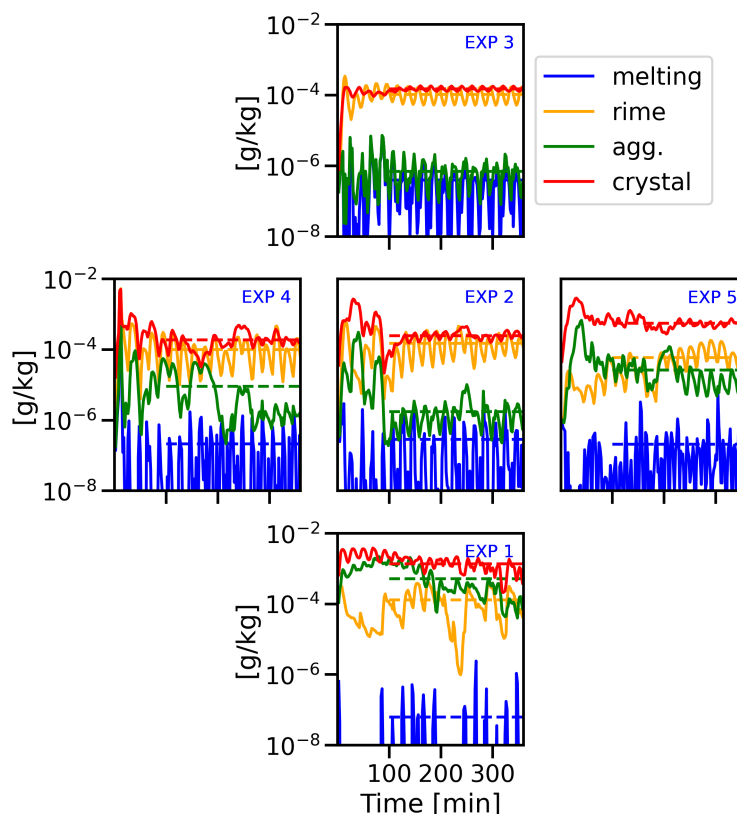
Figure 6. Temporal evolution comparison of the mean mixing ratios of ice processes with the dotted line representing the average value from 100 minutes, including melting, riming, aggregation, and crystal across EXP1–5. The aggregation process is abbreviated "agg.".

The concentration of CCN directly impacts the condensation of water vapor into liquid droplets. With an increase in CCN concentration, a greater number of smaller liquid droplets is formed. However, these smaller droplets have lower inertia and are less effective at colliding with ice particles. As a result, the efficiency of the riming process decreases as the number of small supercooled droplets increases. This observation aligns with previous observation study conducted by Borys et al. (2003). Additionally, the persistence of smaller droplets that freeze before colliding with ice particle and before being able to contribute to riming can grow via the Bergeron-Findeisen process (Bergeron 1935; Findeisen 1938). This process, which operates most efficiently within the temperature range of -15 to $-20\,°C$, occurs in mixed-phase clouds where both supercooled water droplets and ice particles coexist. In the Bergeron-Findeisen process, water vapor tends to preferentially condense onto the ice particles due to the lower saturation vapor pressure over ice compared to water. As a result, the preferential growth of ice particles leads to an increase in the number of ice particles and a decrease in riming. Figure 4 and Figure 5 illustrate how elevated CCN concentrations lead to an increase in the number of ice particles, specifically EXP4 and EXP5, and a decrease in riming efficiency.
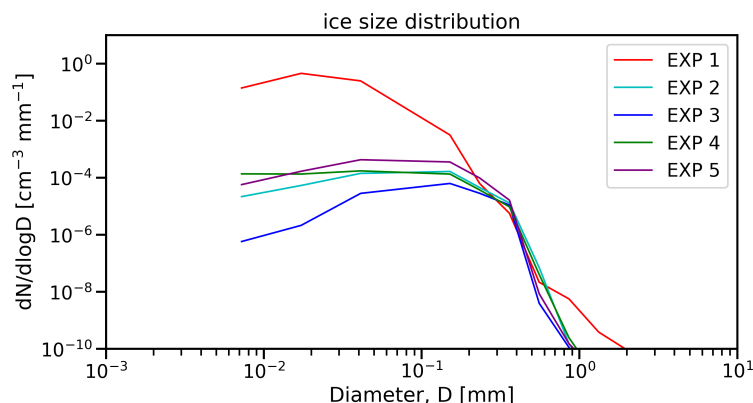
Figure 7. The mean ice particle size distribution averaged after $t = 100$ min.

Therefore, fluctuations in CCN and INP concentrations have significant effects on precipitation formation by modifying the amount of supercooled liquid water. The results indicate that polluted clouds exhibit reduced size and lower amounts of supercooled liquid water, resulting in precipitation primarily formed through ice phase aggregation. Conversely, pristine clouds characterized by larger size and higher amounts of supercooled liquid water predominantly generate precipitation through riming processes.

The frequency of ice particle freezing is influenced by the sizes of liquid particles that freeze most frequently in each scenario. The parameterization of immersion freezing takes into account the volume of the droplets, indicating that larger droplets have a higher probability to freeze. However, the number concentration of the droplets also plays a role, with smaller droplets being more prevalent. Consequently, drawing definitive conclusions about the overall effect becomes challenging. Figure 7 illustrates the size distribution of ice particles based on number weighting. The results demonstrate that an increased concentration of INPs corresponds to a significant abundance of small ice particles. When comparing EXP1 and EXP2, it's worth highlighting that despite EXP1 showing a smaller average size, it still exhibits a substantial population of small particles. This is further compounded by the aggregation process, which plays a pivotal role in transforming these initially smaller hydrometeors into relatively larger ice particles.

In this study, Figure 8 presents the correlation between the number-weighted AR of ice particles and the concentrations of INPs and CCN in mixed-phase clouds. Notably, the results indicate that regardless of the conditions, the ice particles exhibit a plate-like shape with a specific AR within the temperature range from -20 to $-16\,°\mathrm{C}$. Furthermore, the AR decreases as the INP concentration increases. This is attributed to the fact that higher INP concentrations promote the formation of smaller and more compact ice crystals with extreme ARs, in contrast to larger crystals that develop in low INP environments. The smaller-sized crystals exhibit a more pronounced AR due to the non-linear feedback ($\frac{dl_\mathrm{c}}{dl_\mathrm{a}} = \lambda(T)l_\mathrm{c}/l_\mathrm{a}$), where λ represents the inherent growth ratio of ice crystals, reflecting the current atmospheric conditions and the change in the mass of the ice particle (Chen and Lamb, 1994; Hashino and Tripoli, 2007; Hashino et al., 2020).
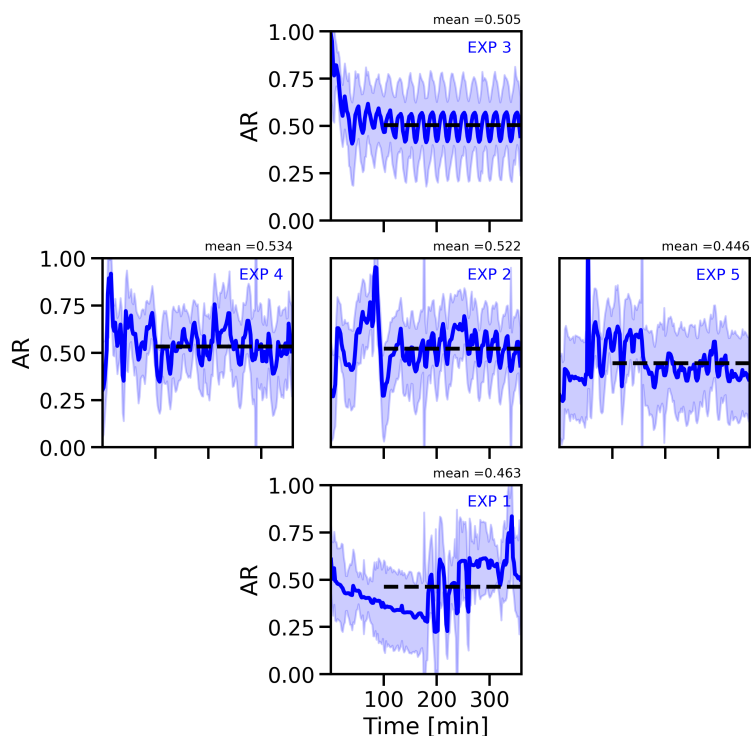
Figure 8. Comparison of the temporal evolution of the mean aspect ratio (AR) with the black dotted line representing the average value from 100 minutes across EXP1–5.

330   Similarly, in the scenario with low CCN concentration (EXP4), ice particles undergo growth through the deposition and riming process, resulting in more spherical shapes. Conversely, in the high CCN scenario, the freezing of droplets through the immersion mode occurs at smaller sizes, leading to the nucleation of smaller ice crystals and the subsequent formation of smaller ice particles. When comparing EXP4 and EXP5 in Figure 7, an increase in CCN concentration is observed to coincide with a significant rise in the concentration of smaller ice particles, accompanied by a decrease in the abundance of

335   larger ice particles around 1 mm. Consequently, the overall average value exhibits an increasing trend with increasing CCN concentration, primarily driven by the greater number of small ice particles. This phenomenon also leads to an increase in ice water mass and the availability of water vapor for ice particle growth, resulting in a higher abundance of small ice particles and a slight decrease in the AR, as illustrated in Figure 8.

    To gain a better understanding of AR, we examined AR with each ice habit in detail. As shown in Figure 9, the ice particles

340   in the mixed-phase clouds, where the temperature ranges from -20 to $-16\,°C$, primarily exhibit a plate-like shape with AR (α) < 1, consisting of plates and irregular polycrystal habits. The result agrees with earlier findings from laboratory studies (Bailey and Hallett, 2009) and observations (Auer and Veal, 1970). Most droplets that freeze close to $-20\,°C$ are polycrystalline in nature, as observed in polycrystalline ice habit frequency from in situ observations (Bailey and Hallett, 2009).
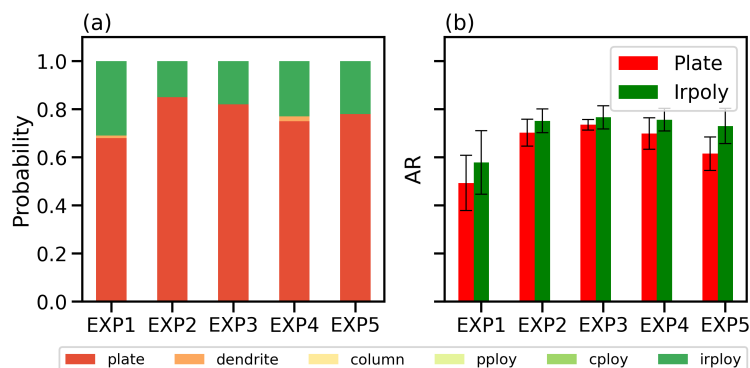
Figure 9. Comparative analysis of the probability of (a) ice habit classification, including plate, dendrite, column, planar polycrystal (pploy), columnar polycrystal (cpoly), and irregular polycrystals (irpoly), and (b) mean AR and standard deviation (with error bars) for plate and irregular polycrystals during the two-hour period following 100 minutes across EXP1–5.

To clarify, in the AMPS model, if the maximum dimension of the ice crystal is less than $20\,\mu m$ and the temperature is

345 below $-20\,°C$, the growth regime is determined using the corresponding cumulative relative frequency of habits and a random number generator. In this case, small ice crystals can exhibit growth modes that differ from the habit diagnosed at the start of the time step. However, for temperatures above $-20\,°C$, it is assumed that polycrystals do not form. Once the maximum dimension of the ice crystal exceeds $20\,\mu m$, it is assumed to follow the growth of the diagnosed habit at the beginning of the time step. These indicate that a majority of the irregular polycrystals observed in this experiment are primarily formed within

350 the initial cloud top layer, where the temperature is approximately near $-20\,°C$.

Figure 9(a) provides insights into the predominant shape of ice particles, with plates representing the majority of the particles. EXP1 exhibits a plate fraction of 68%, while the remaining experiments range from 75% to 85%. As the concentration of INPs increases, a greater number of ice particles form, as shown in Figure 4. Over time, the initially formed plate-shaped ice crystals undergo a transformation influenced by the aggregation process, resulting in the emergence of irregular polycrystals. Notably,

355 the AR of plates gradually decreases compared to that of irregular polycrystals as the INP concentration increases. In EXP1, as depicted in Figure 8, the AR demonstrates an increase after 200 minutes, primarily attributed to the formation of irregular polycrystals. This phenomenon arises from the aggregation process involving newly formed small ice particles and pre-existing ice particles. The resulting irregular polycrystals exhibit a higher AR compared to the plate-shaped crystals, contributing to an overall increase in the average AR. In EXP1, the aggregation process becomes more pronounced, leading to the formation

360 of fully glaciated clouds and a notable increase in the occurrence of irregular polycrystals. A comparison between EXP4 and EXP5 in Figure 9(a) reveals similar proportions of the plate and irregular polycrystal shapes. However, Figure 9(b) shows that the AR is smaller in EXP5. This observation is consistent with previous results, indicating that higher concentrations of CCN lead to higher ice particle concentrations, resulting in a lower AR.

In conclusion, Figure 9 provides compelling evidence of a correlation between the concentration of INPs, CCN, and the AR

365 of ice particles. The findings indicate a decrease in the AR as the concentrations of INPs and CCN increase.
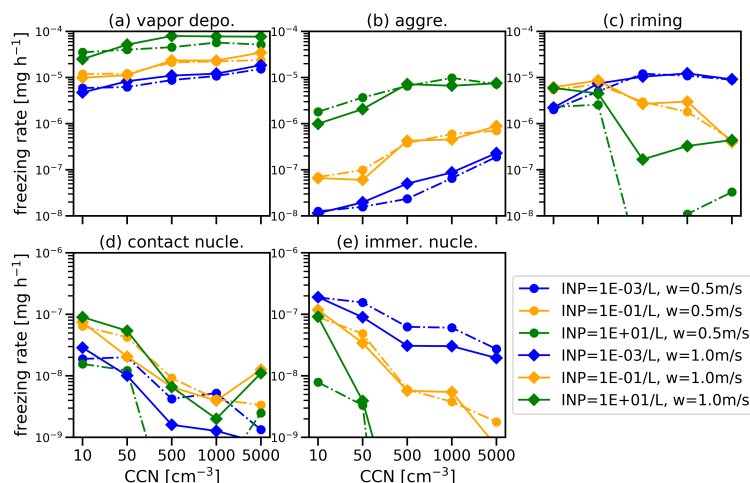
Figure 10. Comparison of mean freezing process rates, including (a) vapor deposition, (b) aggregation, (c) riming, (d) contact nucleation, and (e) immersion nucleation across 15 cases. The model outputs for the process rates are recorded every 1 minute, and the data are spatially averaged over the domain grid points, excluding the first 100 minutes. The dashed line represents the value of w_1 when we decrease from $1.0\,\mathrm{m\,s^{-1}}$ to $0.5\,\mathrm{m\,s^{-1}}$, as defined in Eq. (2).

4.2 Sensitivity test

In Section 4.1 of this study, the primary focus is the analysis and comparison of the five most frequently observed scenarios, exploring the changes observed over the entire duration of the experiment. Now, in Section 4.2, the focus shifts to examining the average values, specifically excluding the initial 100 minutes for each experiment. The objective of this section is to investigate

370   the tendencies and influences of individual ice microphysical processes, as well as to assess the impacts of varying dynamics and initial INP types across a total of 15 setups.

Figure 10 illustrates the mean freezing rate of ice particles under different CCN and INP scenarios. In the AMPS model, the source terms of ice mass include ice nucleation, vapor deposition, aggregation, riming, hydrodynamic breakup, and melting-shedding. In mixed-phase clouds, ice particles primarily grow through vapor deposition, a process in which water vapor

375   molecules freeze onto their surface. According to the experiments, deposition is the primary process for ice growth, further enhanced by increasing CCN and INP concentrations. The riming and aggregation processes are the next significant contributors, followed by the nucleation process. The hydrodynamic breakup and melting-shedding processes are not activated in this experiment.

The increase in INP concentration amplifies the contact nucleation process, aggregation process, and subsequent deposi-

380   tional growth, while the riming-related growth and immersion nucleation process show a decline. At low INP concentrations, the riming-related growth is comparable to deposition. However, as the INP concentration rises, the contribution of riming considerably diminishes, as discussed earlier. Consequently, the availability of liquid becomes a limiting factor for riming. The contribution of riming exhibits a significant decrease with increasing CCN concentration, except in low INP conditions.
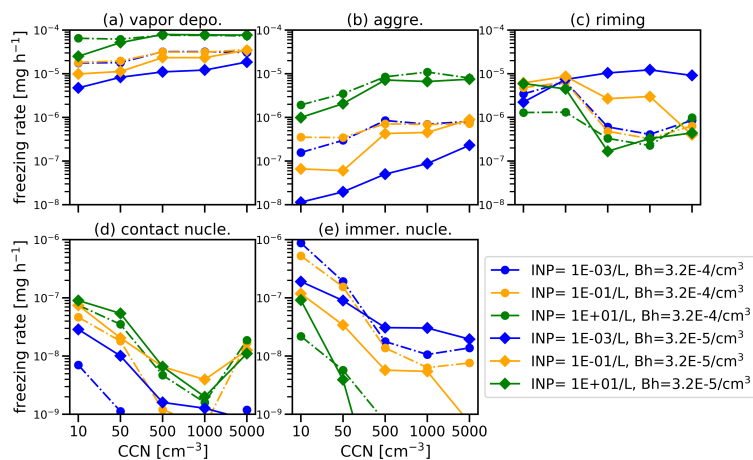
Figure 11. Comparison of the mean freezing process rates, including vapor deposition, riming, contact nucleation, and immersion nucleation, across 15 cases. The data presented in the plots were processed using the same methodology as described in Figure 10. The dashed line in the plots represents the enhanced value of the immersion freezing rate ($Bh = 3.2 \times 10^{-4}$ cm^{-3}) as defined in Eq. (1) in the study by Hashino et al. (2020).

Notably, when a substantial difference exists, the difference can exceed 10 times the values observed in between different scenarios. The major microphysical processes, including vapor deposition, riming, and nucleation, exhibit high sensitivity to INPs. Their sensitivity becomes more significant in high INP conditions, accompanied by significant changes in dynamics and thermodynamics. To investigate the impact of dynamic factors, we decreased w_1 from $1.0\,\mathrm{m\,s^{-1}}$ to $0.5\,\mathrm{m\,s^{-1}}$ in Eq. (2), leveraging the capability of KiD-AMPS to differentiate between dynamic and microphysical effects. The results confirm that an increase in w_1 amplifies the vapor deposition rate, aggregation rate, and contact nucleation processes while reducing the immersion freezing rate. However, the overall trends exhibit a similar pattern.

According to Hashino et al. (2020), the volume-dependent Bigg's immersion method Diehl and S.Wurzler (2004) is a suitable approach for modeling mixed-phase clouds (see Eq. (1) in Hashino et al. (2020)). To account for this information, we adapt Bigg's immersion freezing scheme for our study. In this scheme, the freezing rate is strongly influenced by the droplet mass as well as Bh and Temperature. Bh represents the freezing efficiency of insoluble material in the droplet and is currently set to 3.2×10^{-5}cm^{-3} for montmorillonite, as reported by Diehl and Wurzler (2004). To explore the effects of varying Bh, we multiplied the parameter by a factor of 10 and compared the resulting changes in freezing rates. The findings are presented in Figure 11, indicating that an increase in Bh results in an increase in immersion freezing rate, aggregation production rate, and a minor increase in vapor deposition rate, while the effect of contact nucleation decreases. Nonetheless, the vapor deposition process remains the dominant factor, impacting the AR by reducing it as Bh increases. This is similar to the effect of INP increase, which generates smaller AR ice particles due to an increase in IWC.

The relationship between CCN concentration and the rate of ice production through immersion freezing in mixed-phase clouds is complex and depends on multiple factors. In theory, an increase in CCN concentration can result in the formation

of more cloud droplets. If these droplets become supercooled, they can potentially serve as sites for ice formation through immersion freezing when INPs are present. This suggests a potential increase in the rate of ice production with higher CCN

405 concentration. However, the results reveal a decrease in the contribution of immersion nucleation with increasing CCN concentration. This can be attributed to the twofold effect of increasing CCN. On the one hand, it can lead to a higher number of cloud droplets available for freezing. On the other hand, it tends to produce smaller cloud droplets due to increased competition for available water vapor, known as the Twomey effect (Twomey, 1974). Smaller droplets require colder temperatures to freeze, making them less likely to initiate ice formation. As a result, an increase in CCN concentration does not lead to a corresponding

410 increase in the rate of ice production if the droplets are too small to freeze. Moreover, as the concentration of INP increases, the mass contribution of the immersion freezing rate also decreases. As depicted in Figure 5, an increase in INP concentration leads to a decrease in LWC, as well as a reduction in the areas of ice particles and coexistence. The immersion freezing rate is influenced by the average mass of droplets in the same mass bin and location. Therefore, it is evident that the immersion freezing rate also declines with increasing INP concentrations.

415 To sum up, the relationship between aerosol concentration and the rate of ice production through immersion freezing is intricate and influenced by various factors, including the properties and concentration of CCN and INPs, temperature, and supersaturation level within the cloud. To definitively determine the actual effect of increasing INP and CCN on the rate of ice production through immersion freezing, careful cloud microphysical modeling or observations are necessary.

4.3 PAMTRA coupled with AMPS

420 In this final result section, the application of PAMTRA to the simulations EXP1–5 will be elaborated to demonstrate the sensitivity of radar observations to changes in CCN and INP..

As radar reflectivity is determined by multiple parameters, including size, density, and AR (see Eq. (1)), forward simulations are required in order to evaluate the effects of INP and CCN perturbations on observable parameters such as the radar reflectivity. The results of the forward simulations for the 5 experiments, as explained in Sect. 2.3, are shown in Figure 12.

425 The spectral-bin model reveals a clear decrease in particle size as aerosol loads increase, which leads to a decrease in radar reflectivity due to the strong dependence of backscattering on particle size to the power of 6. However, as shown in Figure 12, the radar reflectivity increases with increasing INP concentrations, which is consistent with observations (Zhang et al., 2018; Radenz et al., 2021) . The increase in reflectivity is attributed not only to changes in particle size but also to alterations in number concentration, AR, and other parameters.

430 In the context of analyzing radar reflectivity data, it is essential to determine the mean vertical profile in order to understand the atmospheric structure and characteristics at various altitudes. This information provides valuable insights into the vertical distribution of hydrometeors. Examining the profiles in Figure 12, we observe a noticeable increase in reflectivity at the cloud bottom (at around 300 m) as the CCN concentration rises. This increase can be attributed to the greater number of cloud droplets resulting from the higher CCN concentration. It is noteworthy that EXP5 displays a remarkably low standard deviation

435 in the cloud bottom at 300 m, indicating a relatively uniform distribution of particle sizes in that region. Consistent with expectations, an increase in the INP concentration leads to elevated reflectivity across different altitude levels, accompanied
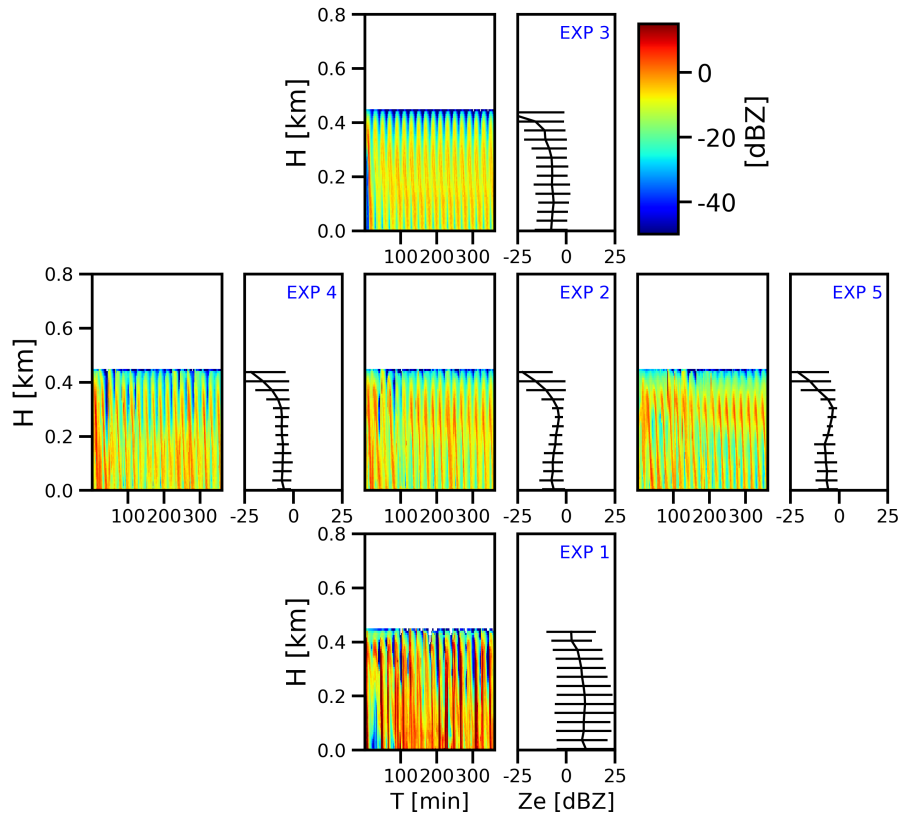
Figure 12. Comparison of the distribution and mean vertical profile of forward-modeled radar reflectivity factor Z_e [dBZ] at Ka-band using the PAMTRA across EXP1–5.

by an increased standard deviation. Higher mean reflectivity values in EXP1 show a larger abundance of hydrometeors in the observed scenarios. However, an intriguing finding is the contrasting pattern observed in the cloud top, where the standard deviation demonstrates a decrease.

Table 2. A comprehensive statistical analysis of the radar reflectivity factor (Z_e) [dBZ] distribution, which includes the computation of mean (μ), standard deviation (σ), and skewness ($\tilde{M}$) values. The data are spatially averaged over the grid points of the domain, excluding the initial 100 minutes.

		CCN [cm^{-3}]		
$(\mu, \sigma, \tilde{M})$		10	50	500
	0.001		EXP3 (-11.83, 9.12, 0.36)	
INP [L^{-1}]	0.1	EXP4 (-10.23, 5.70, 1.63)	EXP2 (-10.09, 5.60, 1.19)	EXP5 (-9.87, 5.05, 1.71)
	10		EXP1 (4.65, 12.47, 2.87)	

440   Table 2 presents the comprehensive statistics of reflectivity, including the total (temporal and vertical) mean (μ), standard deviation (σ), and skewness ($\tilde{M}$). Our examination of radar reflectivity data unveils distinct statistical patterns that are influenced by the concentrations of CCN and INP. For instance, we find that the mean radar reflectivity is -10.09 dBZ, accompanied by a standard deviation of 5.60 dBZ and a skewness of 1.19 for the reference mixed-phase stratocumulus cloud case in EXP2. These values indicate a relatively symmetrical distribution with a slight rightward skew. As the CCN concentration increases

445   while maintaining the same INP level in EXP5, we observe a marginal rise in the mean reflectivity to -9.87 dBZ, a decrease in the standard deviation to 5.0 dBZ, and an increase in the skewness to 1.71, suggesting a more pronounced skewness in the distribution.

On the other hand, where the INP concentration is elevated to $10\,\mathrm{L}^{-1}$ at a CCN concentration of $50\,\mathrm{cm}^{-3}$ in EXP1, we note a significant increasing in the mean reflectivity to 4.65 dBZ, a larger standard deviation of 12.47 dBZ, and a substantially higher

450   skewness of 2.87. These findings signify a more dispersed and highly skewed distribution, possibly indicating the presence of different hydrometeor types and size variations, including precipitation particles. In this study, this is linked to the aggregation of ice particles. Hydrometeors are plate and irregular polycrystals, most of which are plates. However, as depicted in Figure 7, the size distribution of ice particles is quite diverse in EXP1. Conversely, when the INP concentration is very low at $0.001\,\mathrm{L}^{-1}$ while maintaining a CCN concentration of $50\,\mathrm{cm}^{-3}$, the mean radar reflectivity measures -11.83 dBZ, the standard deviation

455   is 9.12 dBZ, and the skewness is 0.36, implying a homogeneous distribution with a slight leftward skew and a low number of ice and liquid particles. Comparing the mean Z values between EXP2 and EXP3 shows minimal differences. However, distinct variations in distribution are observed based on the values of σ and $\tilde{M}$.

5   Summary and conclusions

This study examines how perturbations of CCN and INP concentration affect the shape of ice particles in mixed-phase clouds.

460   The results reveal that both CCN and INP concentrations play a vital role in determining the shape of ice particles and influencing cloud microphysics. The effective diameter of ice particles, which indicates their size, is found to be influenced by the concentrations of CCN and INP. Higher INP concentrations result in smaller effective diameters, while increased CCN concentrations lead to a slight increase in size. The size distribution of ice particles ranges from tens of microns to thousands of microns, consistent with previous observations. Analysis of ice particle shapes shows that plate-like crystal shapes are most

465   common in the temperature range from -20 to $-16\,^\circ$C. However, a significant presence of irregular polycrystals is observed, especially in scenarios with high INP concentrations. The AR of ice particles is affected by both CCN and INP concentrations, with higher concentrations leading to smaller AR values. This indicates that the concentrations of CCN and INP have an impact on the growth and shape of ice particles in mixed-phase clouds. The relationship between CCN concentration and ice particle shape is more complex than that of INP. Increased CCN concentrations promote the formation of more cloud droplets but result

470   in smaller droplet sizes. As a result, the efficiency of the riming process, where supercooled droplets collide with ice particles, decreases with higher CCN concentrations. In conclusion, the concentrations of CCN and INP significantly influence the shape and morphology of ice particles in mixed-phase clouds. Higher INP concentrations lead to smaller and more compact ice

particles, while increased CCN concentrations result in a decrease in the AR of ice particles. These findings highlight the intricate connection between aerosol concentrations, microphysical processes, and ice particle shapes in cloud systems. Accurate
475   modeling and prediction of cloud behavior and precipitation require a comprehensive understanding of these relationships.

In our study, we employed the radar forward simulator PAMTRA to analyze simulation results and derive radar variables, uncovering significant disparities in the findings. When INP concentrations are at low to moderate levels, the mean value of Z_e remains relatively consistent, indicating a stable trend. However, distinct variations are observed in the Z_e distributions characterized by μ, σ, and skew $\tilde{M}$. Therefore, for future observational studies investigating the impact of aerosols on mixed-
480   phase clouds, it is important to consider incorporating Z_e variability, under the condition that the actual cloud conditions align with the assumptions made in our model. In scenarios with substantial differences in INP concentrations, it demonstrates observed discrepancies of 5.5 dB. This finding aligns with the results reported by Radenz et al. (2021), where a difference of 5–10 dB was observed between continental (Leipzig) and pristine (Punta Arenas) locations within specific temperature ranges. Furthermore, their study reveals that the disparity in INP concentrations is at least one order of magnitude higher and has the
485   potential to be even greater if the contribution of continental aerosols in Punta Arenas is lower than the maximum assumed value.

The formation of ice crystals with different ARs has been linked to variations in CCN and INP concentrations. However, it is important to acknowledge that factors such as temperature, humidity, and wind shear can also have a significant influence on ice crystal ARs. Additionally, the choice of modeling schemes can introduce sensitivity to these ratios. Interestingly, our
490   findings show a decrease in AR with increasing INP concentration, which contradicts the results of a previous study by Ong et al. (2022) where an increase in Bh led to an increase in AR. Ong et al. (2022) also discussed the formation of columnnar crystals with an AR greater than 1, which they attributed to slight variations in temperature conditions. Consequently, the AR varied as the INP concentration increased. The complex relationship between ice particle shape and aerosol load is still not fully understood, and further research is needed to unravel the underlying mechanisms governing ice crystal formation and
495   ARs in different environmental contexts.

The research employed the KiD model to investigate cloud microphysics processes, but it is important to consider the limitations of this one-dimensional framework. The simplified nature of the model may not fully capture the complexities and interactions observed in real three-dimensional cloud systems. Additionally, focusing solely on individual microphysics processes within the model might overlook potential uncertainties that arise from the interactions between these processes
500   in larger-scale weather models. It is crucial to interpret the study's findings while recognizing the limitations of the models used and the omission of key processes such as radiation. The KiD model was developed to understand microphysics schemes without the inclusion of dynamic or radiative feedbacks, which play a significant role in cloud layer heating, cooling, and their impact on cloud microphysics and dynamics. Neglecting these processes could lead to inaccuracies in representing cloud temperature, water vapor distribution, and vertical motions within mixed-phase clouds.

505   To address these limitations, future research will explore shape-integrated simulation models AMPS coupled with 3D dynamic cores such as the ICOsahedral Non-hydrostatic (ICON; Zängl et al., 2015) modelling framework. The simulation data can then be compared to observational radar data using a radar-forward simulator, selecting an observation dataset from field

experiments. By incorporating more sophisticated tools and remote sensing techniques, a more comprehensive and accurate analysis of cloud behavior can be achieved. The aim is to enhance cloud simulations by incorporating these processes to improve realism and accuracy.

Code availability. The Kinematic Driver (KiD) model code is available under the link https://github.com/Adehill/KiD-A.git. The simulation results are available under the link https://doi.org/10.5281/zenodo.8257078 (Lee et al., 2023).

Author contributions. JL conducted all simulations, analyzed the data, and drafted the manuscript. JL, PS, and OK contributed initial ideas and designed experiments. PS and HT supervised the work and revised the manuscript. HT provided the AMPS and MM provided the code PAMTRA, and they provided support throughout the work. All authors actively collaborated in the development of the paper and participated in scientific discussions.

Competing interests. The contact author has declared that neither they nor their co-authors have any competing interests.

Acknowledgements. The work leading to this article was funded by the Deutsche Forschungsgemeinschaft (DFG – German Research Foundation) project SPOMC (project number 408027490) which is part of the DFG priority program SPP 2115 PROM (project number 359922472). We acknowledge the provision of additional funding by SPP 2115 PROM for a research stay of JL in Japan, which enabled the initial cooperation with Tempei Hashino, the key developer of AMPS, for the provision of training in using AMPS.

References

525 Ansmann, A., Mamouri, R.-E., Bühl, J., Seifert, P., Engelmann, R., Hofer, J., Nisantzi, A., Atkinson, J. D., Kanji, Z. A., Sierau, B., Vrek-oussis, M., and Sciare, J.: Ice-nucleating particle versus ice crystal number concentration in altocumulus and cirrus layers embedded in Saharan dust: a closure study, Atmospheric Chemistry and Physics, 19, 15 087–15 115, https://doi.org/10.5194/acp-19-15087-2019, 2019.

Atkinson, J. D., Murray, B. J., Woodhouse, M. T., Whale, T. F., Baustian, K. J., Carslaw, K. S., Dobbie, S., O'Sullivan, D., and Malkin, T. L.: The importance of feldspar for ice nucleation by mineral dust in mixed-phase clouds, Nature, 498, 355–358,
530 https://doi.org/10.1038/nature12278, 2013.

Auer, A. H. and Veal, D. L.: The Dimension of Ice Crystals in Natural Clouds, Journal of Atmospheric Sciences, 27, 919–926, https://doi.org/10.1175/1520-0469(1970)027<0919:TDOICI>2.0.CO;2, 1970.

Bailey, M. P. and Hallett, J.: A Comprehensive Habit Diagram for Atmospheric Ice Crystals: Confirmation from the Laboratory, AIRS II, and Other Field Studies, Journal of the Atmospheric Sciences, 66, 2888–2899, https://doi.org/10.1175/2009JAS2883.1, 2009.

535 Baldauf, M., Seifert, A., Förstner, J., Majewski, D., Raschendorfer, M., and Reinhardt, T.: Operational convective-scale numer-ical weather prediction with the COSMO model: Description and sensitivities, Monthly Weather Review, 139, 3887–3905, https://doi.org/10.1175/MWR-D-10-05013.1, 2011.

Barthlott, C. and Hoose, C.: Aerosol Effects on Clouds and Precipitation over Central Europe in Different Weather Regimes, Journal of the Atmospheric Sciences, 75, 4247–4264, https://doi.org/https://doi.org/10.1175/JAS-D-18-0110.1, 2018.

540 Bergeron, T.: On the physics of clouds and precipitation, in: Proces Verbaux de l'Association de Meteorologie, pp. 156–178, Int. Union of Geodesy and Geophys., Paris, 1935.

Bony, S., Stevens, B., W Frierson, D. M., Jakob, C., Kageyama, M., Pincus, R., Shepherd, T. G., Sherwood, S. C., Pier Siebesma, A., Sobel, A. H., Watanabe, M., and Webb, M. J.: Clouds, circulation and climate sensitivity, Nature Publishing Group, 8, https://doi.org/10.1038/NGEO2398, 2015.

545 Borys, R. D., Lowenthal, D. H., Cohn, S. A., and Brown, W. O.: Mountaintop and radar measurements of anthropogenic aerosol effects on snow growth and snowfall rate, Geophysical Research Letters, 30, 5–8, https://doi.org/10.1029/2002gl016855, 2003.

Boucher, O., Randall, D., Artaxo, P., Bretherton, C., Feingold, G., Forster, P., Kerminen, V.-M., Kondo, Y., Liao, H., Lohmann, U., Rasch, P., Satheesh, S. K., Sherwood, S., Stevens, B., and Zhang, X. Y.: Clouds and aerosols, pp. 571–657, Cambridge University Press, Cambridge, UK, https://doi.org/10.1017/CBO9781107415324.016, 2013.

550 Chen, J. and Liu, Y.: New understanding and quantification of the regime dependence of aerosol-cloud interaction for studying aerosol indirect effects, Geophysical Research Letters, 43, 1780–1787, 2016.

Chen, J.-P. and Lamb, D.: The Theoretical Basis for the Parameterization of Ice Crystal Habits: Growth by Vapor Deposition, Journal of Atmospheric Sciences, 51, 1206–1222, https://doi.org/https://doi.org/10.1175/1520-0469(1994)051<1206:TTBFTP>2.0.CO;2, 1994.

Choudhury, G. and Tesche, M.: A first global height-resolved cloud condensation nuclei data set derived from spaceborne lidar measurements,
555 Earth System Science Data Discussions, 2023, 1–22, https://doi.org/10.5194/essd-2023-91, 2023.

Cotton, W. R., Bryan, G. H., and van den Heever, S. C.: Storm and Cloud Dynamics, Academic Press, 2013.

de Boer, G., Hashino, T., and Tripoli, G. J.: Ice nucleation through immersion freezing in mixed-phase stratiform clouds: Theory and numerical simulations, Atmospheric Research, 96, 315–324, https://doi.org/https://doi.org/10.1016/j.atmosres.2009.09.012, 2010.

de Boer, G., Hashino, T., Tripoli, G. J., and Eloranta, E. W.: A numerical study of aerosol influence on mixed-phase stratiform clouds through
560 modulation of the liquid phase, Atmospheric Chemistry and Physics, 13, 1733–1749, https://doi.org/10.5194/acp-13-1733-2013, 2013.

DeMott, P. J., Prenni, A. J., Liu, X., Kreidenweis, S. M., Petters, M. D., Twohy, C. H., Richardson, M. S., Eidhammer, T., and Rogers, D. C.: Predicting global atmospheric ice nuclei distributions and their impacts on climate, Proceedings of the National Academy of Sciences, 107, 11 217–11 222, https://doi.org/10.1073/pnas.0910818107, 2010.

Desai, N., Chandrakar, K. K., Kinney, G., Cantrell, W., and Shaw, R. A.: Aerosol-Mediated Glaciation of Mixed-Phase Clouds: Steady-State Laboratory Measurements, Geophys. Res. Lett., 46, 9154–9162, https://doi.org/10.1029/2019GL083503, 2019.

Diehl, K. and S.Wurzler: Heterogeneous drop freezing in the immersion mode: Model calculations considering soluble and insoluble particles in the drops, Journal of the Atmospheric Sciences, 61, 2063–2072, https://doi.org/10.1175/1520-0469(2004)061<2063:HDFITI>2.0.CO;2, 2004.

Engelmann, R., Ansmann, A., Ohneiser, K., Griesche, H., Radenz, M., Hofer, J., Althausen, D., Dahlke, S., Maturilli, M., Veselovskii, I., Jimenez, C., Wiesen, R., Baars, H., Bühl, J., Gebauer, H., Haarig, M., Seifert, P., Wandinger, U., and Macke, A.: Wildfire smoke, Arctic haze, and aerosol effects on mixed-phase and cirrus clouds over the North Pole region during MOSAiC: an introduction, Atmospheric Chemistry and Physics, 21, 13 397–13 423, https://doi.org/10.5194/acp-21-13397-2021, 2021.

Eriksson, P., Jamali, M., Mendrok, J., Brath, M., Lemke, O., O'Shea, S. J., Thomas, L., and Leinonen, J.: Evaluation of ice cloud representation in the ECMWF and UK Met Office models using airborne lidar and radar measurements, Atmospheric Chemistry and Physics, 15, 7223–7235, 2015.

Fan, J., Leung, L. R., DeMott, P. J., Comstock, J. M., Singh, B., Rosenfeld, D., Tomlinson, J. M., White, A., Prather, K. A., Minnis, P., Ayers, J. K., and Min, Q.: Aerosol impacts on California winter clouds and precipitation during CalWater 2011: local pollution versus long-range transported dust, Atmospheric Chemistry and Physics, 14, 81–101, https://doi.org/10.5194/acp-14-81-2014, 2014.

Fan, J., Ruby Leung, L., Rosenfeld, D., and Demott, P. J.: Effects of cloud condensation nuclei and ice nucleating particles on precipitation processes and supercooled liquid in mixed-phase orographic clouds, Atmospheric Chemistry and Physics, 17, 1017–1035, https://doi.org/10.5194/acp-17-1017-2017, 2017.

Findeisen, W.: Kolloid-meteorologische Vorgänge bei Neiderschlagsbildung, Meteorol. Z., 55, 121–133, 1938.

Fridlind, A. M., Van Diedenhoven, B., Ackerman, A. S., Avramov, A., Mrowiec, A., Morrison, H., Zuidema, P., and Shupe, M. D.: A fire-ACE/SHEBA case study of mixed-phase arctic boundary layer clouds: Entrainment rate limitations on rapid primary ice nucleation processes, Journal of the Atmospheric Sciences, 69, 365–389, https://doi.org/10.1175/JAS-D-11-052.1, 2012.

Hashino, T. and Tripoli, G. J.: The Spectral Ice Habit Prediction System (SHIPS). Part I: Model Description and Simulation of the Vapor Deposition Process, Journal of the Atmospheric Sciences, 64, 2210–2237, https://doi.org/https://doi.org/10.1175/JAS3963.1, 2007.

Hashino, T. and Tripoli, G. J.: The Spectral Ice Habit Prediction System (SHIPS). Part II: Simulation of Nucleation and Depositional Growth of Polycrystals, Journal of the Atmospheric Sciences, 65, 3071–3094, https://doi.org/https://doi.org/10.1175/2008JAS2615.1, 2008.

Hashino, T. and Tripoli, G. J.: The Spectral Ice Habit Prediction System (SHIPS). Part III: Description of the Ice Particle Model and the Habit-Dependent Aggregation Model, Journal of the Atmospheric Sciences, 68, 1125–1141, https://doi.org/https://doi.org/10.1175/2011JAS3666.1, 2011a.

Hashino, T. and Tripoli, G. J.: The Spectral Ice Habit Prediction System (SHIPS). Part IV: Box Model Simulations of the Habit-Dependent Aggregation Process, Journal of the Atmospheric Sciences, 68, 1142–1161, https://doi.org/https://doi.org/10.1175/2011JAS3667.1, 2011b.

Hashino, T., De Boer, G., Okamoto, H., and Tripoli, G. J.: Relationships between immersion freezing and crystal habit for arctic mixed-phase clouds-A numerical study, Journal of the Atmospheric Sciences, 77, 2411–2438, https://doi.org/10.1175/JAS-D-20-0078.1, 2020.

Heymsfield, A. and Westbrook, C.: A review of cloud particle types in storms and their contributions to rainfall and snowfall, Atmospheric Research, 97, 273–282, 2010.

Heyn, I., Block, K., Mülmenstädt, J., Gryspeerdt, E., Kühne, P., Salzmann, M., and Quaas, J.: Assessment of simulated aerosol effective
600   radiative forcings in the terrestrial spectrum, Geophysical Research Letters, 44, 1001–1007, https://doi.org/10.1002/2016GL071975, 2017.

Hogan, R. J., Illingworth, A. J., Sauvageot, H., and Gaussiat, N.: Stratocumulus Liquid Water Content from Dual-Wavelength Radar, Journal
of Atmospheric and Oceanic Technology, 17, 379–386, 2000.

Hogan, R. J., Westbrook, C. D., Illingworth, A. J., Wood, C. R., and Donovan, D. P.: A Variational Scheme for Retrieving Ice Cloud Properties
from Combined Radar, Lidar, and Infrared Radiometer, Journal of the Atmospheric Sciences, 69, 634–654, 2012.

605   Hogan, R. J., Honeyager, R., Tyynelä, J., and Kneifel, S.: Calculating the Millimetre-Wave Scattering Phase Function of Snowflakes Using
the Self-Similar Rayleigh–Gans Approximation, Q. J. Roy. Meteor. Soc., 143, 834–844, https://doi.org/10.1002/qj.2968, 2017.

Hoose, C. and Möhler, O.: Heterogeneous ice nucleation on atmospheric aerosols: A review of results from laboratory experiments, vol. 12,
https://doi.org/10.5194/acp-12-9817-2012, 2012.

Kahn, R. A., Andrews, E., Brock, C. A., Chin, M., Feingold, G., Gettelman, A., Levy, R. C., Murphy, D. M., Nenes, A., Pierce, J. R.,
610   Popp, T., Redemann, J., Sayer, A. M., da Silva, A. M., Sogacheva, L., and Stier, P.: Reducing Aerosol Forcing Uncertainty by Combining
Models With Satellite and Within-The-Atmosphere Observations: A Three-Way Street, Reviews of Geophysics, 61, e2022RG000 796,
https://doi.org/https://doi.org/10.1029/2022RG000796, 2023.

Kanji, Z. A., Ladino, L. A., Wex, H., Boose, Y., Burkert-Kohn, M., Cziczo, D. J., and Krämer, M.: Overview of Ice Nucleating Particles,
Meteorological Monographs, 58, 1.1—-1.33, 2017.

615   Klein, S. A., McCoy, R. B., Morrison, H., Ackerman, A. S., Avramov, A., de Boer, G., Chen, M., Cole, J. N. S., Del Genio, A. D.,
Falk, M., Foster, M. J., Fridlind, A., Golaz, J.-C., Hashino, T., Harrington, J. Y., Hoose, C., Khairoutdinov, M. F., Larson, V. E., Liu,
X., Luo, Y., McFarquhar, G. M., Menon, S., Neggers, R. A. J., Park, S., Poellot, M. R., Schmidt, J. M., Sednev, I., Shipway, B. J.,
Shupe, M. D., Spangenberg, D. A., Sud, Y. C., Turner, D. D., Veron, D. E., von Salzen, K., Walker, G. K., Wang, Z., Wolf, A. B.,
Xie, S., Xu, K.-M., Yang, F., and Zhang, G.: Intercomparison of model simulations of mixed-phase clouds observed during the ARM
620   Mixed-Phase Arctic Cloud Experiment. I: single-layer cloud, Quarterly Journal of the Royal Meteorological Society, 135, 979–1002,
https://doi.org/https://doi.org/10.1002/qj.416, 2009.

Kneifel, S., Redl, S., Orlandi, E., Löhnert, U., Cadeddu, M. P., Turner, D. D., and Chen, M.: Snow Scattering Signals in Ground-Based
Passive Microwave Radiometer Measurements, Journal of Applied Meteorology and Climatology, 54, 1712–1729, 2015.

Liou, K.-N. and Ou, S. S. C.: Light scattering by ice crystals: fundamentals and applications, Progress in Energy and Combustion Science,
625   30, 267–306, 2004.

Maahn, M., Hoffmann, F., Shupe, M. D., de Boer, G., Matrosov, S. Y., and Luke, E. P.: Can liquid cloud microphysi-
cal processes be used for vertically pointing cloud radar calibration?, Atmospheric Measurement Techniques, 12, 3151–3171,
https://doi.org/https://doi.org/10.5194/amt-12-3151-2019, 2019.

Magono, C. and Lee, C. W.: Meteorological classification of natural snow crystals, Journal of the Faculty of Science, Hokkaido University.
630   Series 7, Geophysics, 2, 321–335, 1966.

Maherndl, N., Maahn, M., Tridon, F., Leinonen, J., Ori, D., and Kneifel, S.: A riming-dependent parameterization of scattering by snowflakes
using the self-similar Rayleigh–Gans Approximation, Q.J.R. Meteorol. Soc., in review, 2023.

Matsui, T., Iguchi, T., Li, X., Han, M.-I., Tao, W.-K., Peters-Lidard, C., Kummerow, C., Lang, S., Meneghini, R., and Liao, L.: Evaluation of
cloud microphysics schemes in simulations of a winter storm using radar and radiometer measurements, Journal of Geophysical Research:
635   Atmospheres, 124, 639–663, 2019.

McFarquhar, G. M. and Heymsfield, A. J.: Parameterization of Tropical Cirrus Ice Crystal Size Distributions and Implications for Radiative Transfer: Method and Preliminary Results, Journal of the Atmospheric Sciences, 54, 2187–2200, 1997.

Mech, M., Maahn, M., Kneifel, S., Ori, D., Orlandi, E., Kollias, P., Schemann, V., and Crewell, S.: PAM-TRA 1.0: the Passive and Active Microwave radiative TRAnsfer tool for simulating radiometer and radar measurements of the cloudy atmosphere, Geoscientific Model Development, 13, 4229–4251, https://doi.org/10.5194/gmd-13-4229-2020, 2020.

Mishchenko, M. I., Travis, L. D., and Lacis, A. A.: Scattering, Absorption, and Emission of Light by Small Particles, 1996.

Mitchell, D. L.: Use of Mass- and Area-Dimensional Power Laws for Determining Precipitation Particle Terminal Velocities, Journal of the Atmospheric Sciences, 53, 1710–1723, 1996.

Morrison, H., Curry, J. A., and Khvorostyanov, V. I.: A New Double-Moment Microphysics Parameterization for Application in Cloud and Climate Models. Part I: Description, Journal of the Atmospheric Sciences, 62, 1665–1677, 2005.

Morrison, H., Thompson, G., and Tatarskii, V.: Impact of cloud microphysics on the development of trailing stratiform precipitation in a simulated squall line: Comparison of one- and two-moment schemes, Monthly Weather Review, 137, 991–1007, https://doi.org/10.1175/2008MWR2556.1, 2009.

Morrison, H., Zuidema, P., Ackerman, A. S., Avramov, A., de Boer, G., Fan, J., Fridlind, A. M., Hashino, T., Harrington, J. Y., Luo, Y., Ovchinnikov, M., and Shipway, B.: Intercomparison of cloud model simulations of Arctic mixed-phase boundary layer clouds observed during SHEBA/FIRE-ACE, Journal of Advances in Modeling Earth Systems, 3, https://doi.org/https://doi.org/10.1029/2011MS000066, 2011.

Morrison, H., de Boer, G., Feingold, G., Harrington, J., Shupe, M. D., and Sulia, K.: Resilience of persistent Arctic mixed-phase clouds, Nature Geoscience, 5, 11–17, https://doi.org/10.1038/ngeo1332, 2012.

Mülmenstädt, J., Stevens, B., and Bony, S.: Cloud-top radiative cooling: a factor to be considered in convective self-aggregation, Journal of Advances in Modeling Earth Systems, 7, 700–714, 2015.

Ong, C. R., Koike, M., Hashino, T., and Miura, H.: Modeling Performance of SCALE-AMPS: Simulations of Arctic Mixed-Phase Clouds Observed During SHEBA, Journal of Advances in Modeling Earth Systems, 14, 1–22, https://doi.org/10.1029/2021ms002887, 2022.

Ori, D., Schemann, V., Karrer, M., and et al.: Evaluation of ice particle growth in ICON using statistics of multi-frequency Doppler cloud radar observations, QJR Meteorol Soc., 146, 3830–3849, https://doi.org/10.1002/qj.3875, 2020.

Possner, A., Ekman, A. M., and Lohmann, U.: Cloud response and feedback processes in stratiform mixed-phase clouds perturbed by ship exhaust, Geophysical Research Letters, 44, 1964–1972, https://doi.org/10.1002/2016GL071358, 2017.

Radenz, M., Bühl, J., Seifert, P., Baars, H., Engelmann, R., Barja González, B., Mamouri, R. E., Zamorano, F., and Ansmann, A.: Hemispheric contrasts in ice formation in stratiform mixed-phase clouds: disentangling the role of aerosol and dynamics with ground-based remote sensing, Atmospheric Chemistry and Physics, 21, 17 969–17 994, https://doi.org/10.5194/acp-21-17969-2021, 2021.

Schnitt, S., Löhnert, U., and Preusker, R.: Potential of Dual-Frequency Radar and Microwave Radiometer Synergy for Water Vapor Profiling in the Cloudy Trade Wind Environment, Journal of Atmospheric and Oceanic Technology, 37, 1973–1986, https://doi.org/https://doi.org/10.1175/JTECH-D-19-0110.1, 2020.

Seifert, A. and Beheng, K. D.: A two-moment cloud microphysics parameterization for mixed-phase clouds. Part 1: Model description, Meteorology and Atmospheric Physics, 92, 45–66, https://doi.org/10.1007/s00703-005-0112-4, 2006.

Seifert, A., Köhler, C., and Beheng, K. D.: Aerosol-cloud-precipitation effects over Germany as simulated by a convective-scale numerical weather prediction model, Atmospheric Chemistry and Physics, 12, 709–725, 2012.

Seifert, P., Ansmann, A., Mattis, I., Wandinger, U., Tesche, M., Engelmann, R., Müller, D., Pérez, C., and Haustein, K.: Saharan dust and
heterogeneous ice formation: Eleven years of cloud observations at a central European EARLINET site, Journal of Geophysical Research:
Atmospheres, 115, https://doi.org/https://doi.org/10.1029/2009JD013222, 2010.

Shipway, B. J. and Hill, A. A.: Diagnosis of systematic differences between multiple parametrizations of warm rain microphysics using a
kinematic framework, Quarterly Journal of the Royal Meteorological Society, 138, 2196–2211, https://doi.org/10.1002/qj.1913, 2012.

Solomon, A., de Boer, G., Creamean, J. M., McComiskey, A., Shupe, M. D., Maahn, M., and Cox, C.: The relative impact of cloud conden-
sation nuclei and ice nucleating particle concentrations on phase partitioning in arctic mixed-phase stratocumulus clouds, Atmospheric
Chemistry and Physics, 18, 17 047–17 059, https://doi.org/10.5194/acp-18-17047-2018, 2018.

Tao, W. K., Chen, J. P., Li, Z., Wang, C., and Zhang, C.: Impact of aerosols on convective clouds and precipitation, Reviews of Geophysics,
50, https://doi.org/10.1029/2011RG000369, 2012.

Thompson, G., Rasmussen, R. M., and Manning, K.: Explicit Forecasts of Winter Precipitation Using an Improved
Bulk Microphysics Scheme. Part I: Description and Sensitivity Analysis, Monthly Weather Review, 132, 519–542,
https://doi.org/https://doi.org/10.1175/1520-0493(2004)132<0519:EFOWPU>2.0.CO;2, 2004.

Thompson, G., Field, P. R., Rasmussen, R. M., and Hall, W. D.: Explicit Forecasts of Winter Precipitation Using an Improved
Bulk Microphysics Scheme. Part II: Implementation of a New Snow Parameterization, Monthly Weather Review, 136, 5095–5115,
https://doi.org/10.1175/2008MWR2387.1, 2008.

Twomey, S.: Pollution and the planetary albedo, Atmospheric Environment (1967), 8, 1251–1256,
https://doi.org/https://doi.org/10.1016/0004-6981(74)90004-3, 1974.

Tzivion, S., Feingold, G., and Levin, Z.: An Efficient Numerical Solution to the Stochastic Collection Equation, Journal of Atmospheric
Sciences, 44, 3139–3149, https://doi.org/https://doi.org/10.1175/1520-0469(1987)044<3139:AENSTT>2.0.CO;2, 1987.

Ulaby, F. T., Moore, R. K., and Fung, A. K.: Microwave Remote Sensing: Active and Passive, Artech House, London, 1981.

Um, J. and McFarquhar, G. M.: An update on the ice particle scattering database for radiative transfer studies, Journal of Quantitative
Spectroscopy and Radiative Transfer, 112, 650–652, 2011.

Vázquez-Martín, S., Kuhn, T., and Eliasson, S.: Shape dependence of snow crystal fall speed, Atmospheric Chemistry and Physics, 21,
7545–7565, https://doi.org/10.5194/acp-21-7545-2021, 2021.

von Lerber, A., Mech, M., Rinke, A., Zhang, D., Lauer, M., Radovan, A., Gorodetskaya, I., and Crewell, S.: Evaluating seasonal
and regional distribution of snowfall in regional climate model simulations in the Arctic, Atmos. Chem. Phys., 22, 7287–7317,
https://doi.org/10.5194/acp-22-7287-2022, 2022.

Westbrook, C. D. and Illingworth, A. J.: The fall speeds of sub-100 μm ice crystals, Quarterly Journal of the Royal Meteorological Society,
137, 1266–1281, 2011.

Zängl, G., Reinert, D., Rípodas, P., and Baldauf, M.: The ICON (ICOsahedral Non-hydrostatic) modelling framework of DWD and
MPI-M: Description of the non-hydrostatic dynamical core, Quarterly Journal of the Royal Meteorological Society, 141, 563–579,
https://doi.org/https://doi.org/10.1002/qj.2378, 2015.

Zhang, D., Wang, Z., Kollias, P., Vogelmann, A. M., Yang, K., and Luo, T.: Ice particle production in mid-level stratiform mixed-phase
clouds observed with collocated A-Train measurements, Atmospheric Chemistry and Physics, 18, 4317–4327, https://doi.org/10.5194/acp-
18-4317-2018, 2018.